Cellular/Molecular

Functional Microstructure of Ca$_V$-Mediated Calcium Signaling in the Axon Initial Segment

Anna M. Lipkin,[1] Margaret M. Cunniff,[1] Perry W. E. Spratt,[1] Stefan M. Lemke,[1] and ⬤Kevin J. Bender[1,2]
[1]Neuroscience Graduate Program, University of California, San Francisco, California 94158, and [2]Department of Neurology, Kavli Institute for Fundamental Neuroscience, Weill Institute for Neurosciences, University of California, San Francisco, California 94158

The axon initial segment (AIS) is a specialized neuronal compartment in which synaptic input is converted into action potential (AP) output. This process is supported by a diverse complement of sodium, potassium, and calcium channels (Ca$_V$). Different classes of sodium and potassium channels are scaffolded at specific sites within the AIS, conferring unique functions, but how calcium channels are functionally distributed within the AIS is unclear. Here, we use conventional two-photon laser scanning and diffraction-limited, high-speed spot two-photon imaging to resolve AP-evoked calcium dynamics in the AIS with high spatiotemporal resolution. In mouse layer 5 prefrontal pyramidal neurons, calcium influx was mediated by a mix of Ca$_V$2 and Ca$_V$3 channels that differentially localized to discrete regions. Ca$_V$3 functionally localized to produce nanodomain hotspots of calcium influx that coupled to ryanodine-sensitive stores, whereas Ca$_V$2 localized to non-hotspot regions. Thus, different pools of Ca$_V$s appear to play distinct roles in AIS function.

Key words: two-photon; action potential; axon initial segment; calcium channel; electrophysiology; sodium channel

Significance Statement

The axon initial segment (AIS) is the site where synaptic input is transformed into action potential (AP) output. It achieves this function through a diverse complement of sodium, potassium, and calcium channels (Ca$_V$). While the localization and function of sodium channels and potassium channels at the AIS is well described, less is known about the functional distribution of Ca$_V$s. We used high-speed two-photon imaging to understand activity-dependent calcium dynamics in the AIS of mouse neocortical pyramidal neurons. Surprisingly, we found that calcium influx occurred in two distinct domains: Ca$_V$3 generates hotspot regions of calcium influx coupled to calcium stores, whereas Ca$_V$2 channels underlie diffuse calcium influx between hotspots. Therefore, different Ca$_V$ classes localize to distinct AIS subdomains, possibly regulating distinct cellular processes.

Introduction

Voltage-gated calcium channels (Ca$_V$s) occupy a unique functional niche in neurons, affecting both electrical signaling across the membrane and initiating intracellular cascades that regulate ion channel function, cellular processes, and gene expression. Ca$_V$s are distributed broadly across somatodendritic and axonal compartments, but only recently have we come to appreciate their role at the intersection of these two compartments, the

axon initial segment (AIS). The AIS is enriched with sodium and potassium channels scaffolded by a complex intracellular skeleton and can be a site for specialized inhibitory synaptic input (Bender and Trussell, 2012; Kole and Stuart, 2012; Huang and Rasband, 2018; Leterrier, 2018). Of all Ca$_V$ classes, low voltage-activated Ca$_V$3s appear to be most commonly expressed in the AIS. AIS Ca$_V$3 channels were first shown to regulate the threshold and timing of APs in auditory brainstem cartwheel interneurons, somatosensory cortex pyramidal cells, and cerebellar Purkinje cells (Bender and Trussell, 2009; Bender et al., 2012). AIS-localized Ca$_V$3 channels have also been identified at the AIS of cells in avian brainstem and murine cerebellum, hippocampus, and frontal cortex (Martinello et al., 2015; Clarkson et al., 2017; Dumenieu et al., 2018; Fukaya et al., 2018; Hu and Bean, 2018; Jing et al., 2018). In many of these cells, Ca$_V$3 channels appear to be interspersed in the AIS with other Ca$_V$ classes. This diversity is most apparent in neocortical pyramidal cells, where calcium influx has been reported to be mediated by a range of channel types, including Ca$_V$1, members of the Ca$_V$2 family, and Ca$_V$3 (Clarkson et al., 2017; Hanemaaijer et al., 2020; Yu et al., 2010).

Across neuronal compartments, the spatial organization of Ca_Vs shapes function by linking spatially-restricted calcium influx to nearby calcium-sensitive processes. In somatodendritic compartments, coupling of Ca_Vs to calcium-activated potassium channels regulates action potential (AP) dynamics (Bock and Stuart, 2016; Irie and Trussell, 2017), EPSP amplitude and summation (Wang et al., 2014; Chen-Engerer et al., 2019), and calcium influx (Jones and Stuart, 2013). In the soma, calcium influx through Ca_V1 channels influences activity-dependent transcription by nuclear transcription factors through activation of CREB via CaMKII (Wheeler et al., 2012). And in axon terminals, the density and spatial arrangement of Ca_Vs relative to neurotransmitter release machinery determines release probability (Scimemi and Diamond, 2012; Rebola et al., 2019), shaping both the dynamics of short-term plasticity and its regulation by neuromodulators (Bucurenciu et al., 2008; Vyleta and Jonas, 2014; Burke et al., 2018). However, the organization of Ca_Vs within the AIS, and how they interact with calcium sensitive signaling pathways, remains unclear.

The AIS serves multiple roles, acting both as a site of electrogenesis for APs as well as a diffusion barrier between somatodendritic and axonal compartments (Bender and Trussell, 2012; Leterrier and Dargent, 2014). These functions are supported by a complex scaffold of intracellular and membrane-bound proteins. Rings of actin connected by spectrins occur periodically along the AIS, forming a scaffold for ankyrin-G to bind and anchor voltage-gated sodium channels (Na_V) and voltage-gated potassium (K_V) K_V7 channels (Leterrier, 2018). $K_V1.1$ and $K_V1.2$ are anchored by a complex that includes PSD-93 and the paranodal protein Caspr and typically cluster at actin rings (Ogawa and Rasband, 2008; Pinatel et al., 2017). $K_V2.1$ channels are found at yet another clustering domain enriched with the scaffolding protein gephyrin (King et al., 2014). In neocortical pyramidal cells, these gephyrin-rich sites are punctate, occupying small gaps in an otherwise continuous sheath of Na_V-rich membrane. It is here that chandelier cells form GABAergic synapses at the AIS (Inan and Anderson, 2014). Furthermore, a specialized endoplasmic reticulum, termed the cisternal organelle, abuts these gephyrin-rich regions. These cisternal organelles express ryanodine receptors (RyRs; King et al., 2014), which mediate calcium-induced calcium release from intracellular stores. Interestingly, we have previously shown that RyR-dependent signaling is necessary for dopaminergic signaling cascades that regulate AIS Ca_V3 function (Yang et al., 2016), but the local calcium source that evokes calcium-induced calcium release at these sites has not been identified. Given the differential distribution of other ion channel classes in the AIS (Lorincz and Nusser, 2008), we hypothesized that a unique complement of Ca_Vs may be localized to these regions and engage RyRs.

Here, we developed diffraction-limited, high-frequency two-photon imaging techniques to explore the functional microstructure of AP-evoked calcium signaling in mouse prefrontal pyramidal cell initial segments. We found that calcium influx occurred during AP repolarization, and was distinct from sodium influx occurring during the rising phase of the AP (Pressler and Strowbridge, 2019; Filipis and Canepari, 2021; but see Hanemaaijer et al., 2020). Calcium influx was mediated by a mix of $Ca_V2.1$, $Ca_V2.2$, $Ca_V2.3$, and Ca_V3 calcium channels that were distributed into distinct functional domains. In some regions, micron-wide "hotspots" of fast, high-amplitude calcium influx occurred. These hotspots were dominated by Ca_V3-mediated calcium influx, whereas non-hotspot regions were dominated by $Ca_V2.1/2.2$-mediated influx. Furthermore, Ca_V3 channels were preferentially linked to RyR-

dependent intracellular stores, suggesting that AIS Ca_V3 channels, commonly expressed in many neuronal classes, are complexed in pyramidal cells to regions associated with GABAergic synaptic transmission. Thus, Ca_Vs may play distinct roles in different subcompartments within the AIS.

Materials and Methods

Ex vivo *electrophysiological recordings*

All experiments were performed in accordance with guidelines set by the University of California Animal Care and Use Committee. C57Bl/6 mice of both sexes aged postnatal day (P)20 through P30 were anesthetized and 250-μm coronal sections containing medial prefrontal cortex were collected. Cutting solution contained the following: 87 mM NaCl, 25 mM $NaHCO_3$, 25 mM glucose, 75 mM sucrose, 2.5 mM KCl, 1.25 mM NaH_2PO_4, 0.5 mM $CaCl_2$, and 7 mM $MgCl_2$, bubbled with 5% CO_2/95% O_2. After cutting, slices were incubated in the same solution for 30 min at 33°C, then at room temperature until recording. Recording solution contained the following: 125 mM NaCl, 2.5 mM KCl, 2 mM $CaCl_2$, 1 mM $MgCl_2$, 25 mM $NaHCO_3$, 1.25 mM NaH_2PO_4, and 25 mM glucose, bubbled with 5% CO_2/95% O_2. Recordings were done at 32–34°C, with the exception of SBFI and Fluo4ff experiments, which were performed at room temperature (22°C). Osmolarity of the recording solution was adjusted to ~310 mOsm.

Neurons were visualized using Dodt contrast optics for visually-guided whole-cell recording. Patch electrodes were pulled from Schott 8250 glass (3–4 MΩ tip resistance) and filled with a solution containing the following: 113 mM K-gluconate, 9 mM HEPES, 4.5 mM $MgCl_2$, 14 mM $Tris_2$-phoshocreatine, 4 mM Na_2-ATP, and 0.3 mM Tris-GTP, ~290 mOsm, pH 7.2–7.25. Calcium buffers, volume filling dyes, and calcium or sodium indicators were included in the internal solution as follows: for linescan calcium imaging experiments, 250 μM Fluo-5F and 20 μM Alexa Fluor 594 were added. For fast (5.3 kHz) linescan sodium imaging, 2 mM SBFI, 0.1 μM EGTA, and 20 μM Alexa Fluor 594 were added. For fast linescan calcium imaging, 500 μM Fluo-4FF and 0.1 μM EGTA were added. For calcium imaging at single diffraction limited spots, 600 μM OGB-5N, 0.1 μM EGTA and 20 μM Alexa Fluor 594 were added. For pointscan sodium imaging, 500 μM ING-2 was added.

Electrophysiological data were acquired using a Multiclamp 700B amplifier (Molecular Devices). For fast linescan experiments, data were acquired at 50 kHz and filtered at 20 kHz. For all other experiments, data were acquired at 20 kHz and filtered at 10 kHz. All recordings were made using a quartz electrode holder to eliminate electrode drift within the slice, enabling stable imaging of diffraction-limited spots in close proximity to the recording electrode (Sutter Instruments). Cells were excluded if series resistance exceeded 20 MΩ or if the series resistance changed by >30%. All recordings were made from layer 5b pyramidal neurons in prefrontal or primary somatosensory cortex and data were corrected for a 12-mV junction potential.

Two-photon imaging

Two-photon laser-scanning microscopy (2PLSM) was performed as described previously (Bender and Trussell, 2009). A Coherent Ultra II laser was tuned to 810 nm for morphology and calcium imaging and ING-2-based sodium imaging. The laser was tuned to 790 nm for SBFI-based imaging. Fluorescence was collected with either a 40×, 0.8 NA objective (data in Figs. 1-3) or a 60×, 1.0 NA objective (data in Figs. 4-6) paired with a 1.4 NA oil immersion condenser (Olympus). Dichroic mirrors and bandpass filters (575 DCXR, ET525/70 m-2p, ET620/60 m-2p, Chroma) were used to split fluorescence into red and green channels unless otherwise specified. HA10770-40 photomultiplier tubes (PMTs, Hamamatsu) selected for >50% quantum efficiency and low dark counts captured green fluorescence (Fluo-5F, Fluo-4FF, OGB-5N). Red fluorescence (Alexa Fluor 594) was captured using R9110 PMTs. For ING-2-based imaging, the epifluorescence filters were removed and the trans-fluorescence filters were replaced with a single 535/150 bandpass filter (Semrock) and all fluorescence was collected on HA10770-40 PMTs.

Fluorescence data were collected either using linescan or pointscan configurations. In linescan mode, the laser was repeatedly scanned over
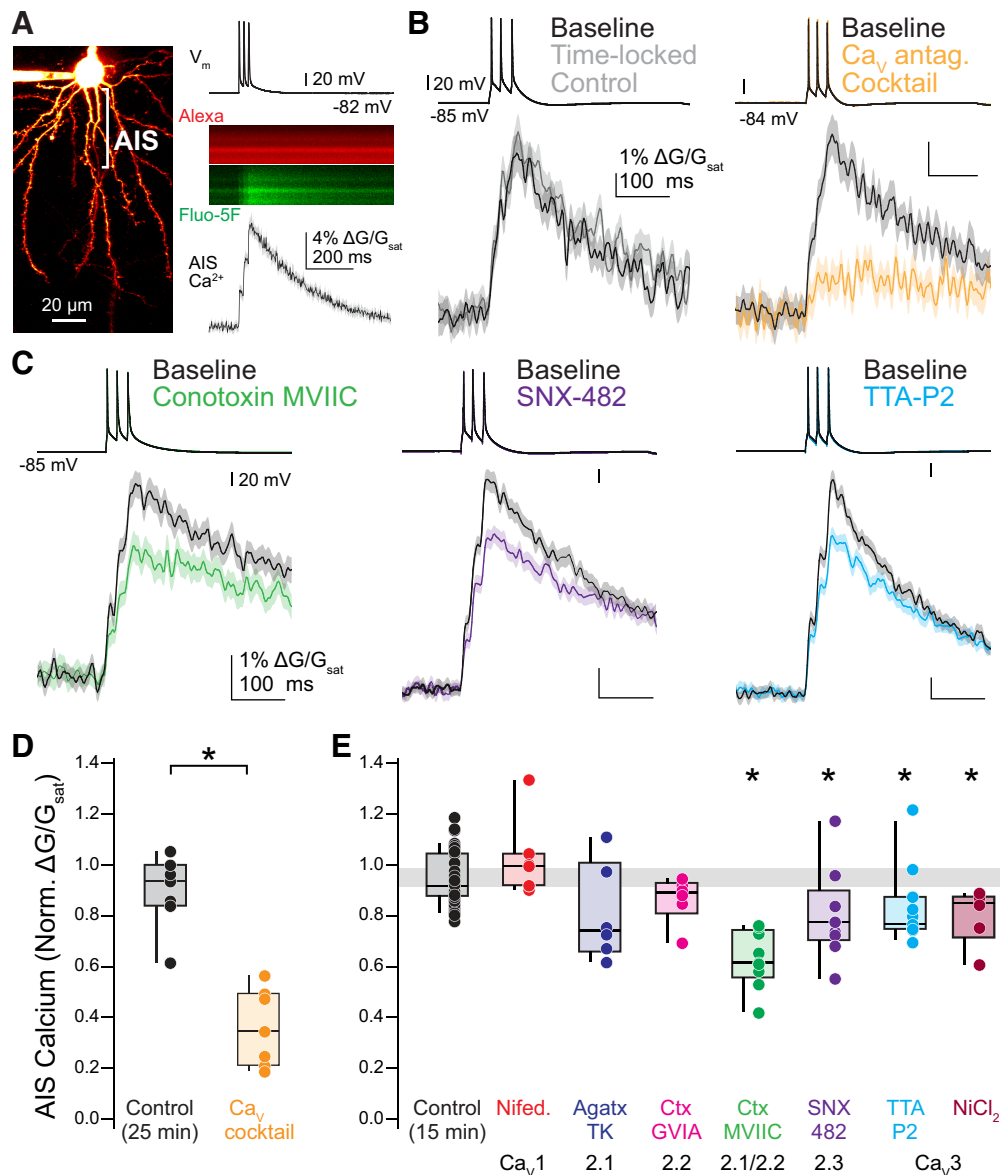
Figure 1. $Ca_V2.1$, $Ca_V2.2$, and Ca_V3 contribute to calcium influx at the AIS. ***A***, left, 2PLSM z-stack of a layer 5 pyramidal neuron visualized with Alexa Fluor 594. AIS indicated by bracket. Right, Example linescan of AIS averaged over 20 trials. APs were evoked with somatic current injection (1 nA, 5 ms, 20-ms interstimulus interval). ***B***, left, Representative time-locked control cell. Linescan data displayed as mean ± SE. Baseline, black; post, gray. Right, Representative effects of Ca_V antagonist cocktail on AIS calcium. Baseline, black; cocktail, yellow. ***C***, Representative examples of selective Ca_V antagonists on AIS calcium. Baseline, black; antagonists, other colors. ***D***, Summary of the effects of the Ca_V antagonist cocktail on AIS calcium. *$p < 0.05$, Mann-Whitney U test. ***E***, Summary of the effects of individual Ca_V antagonists on AIS calcium. Gray bar represents 95% confidence interval of control data. $p < 0.05$, Kruskal-Wallis with Mann-Whitney U test post hoc.

a region of axon at a rate of ~0.5 or 5.3 kHz. For 0.5-kHz calcium imaging, data were averaged over 20–40 trials and reported as $\Delta G/G_{sat}$, which was calculated as $\Delta(G/R)/(G/R)_{max}*100$, where G/R_{max} is the maximal fluorescence in saturating calcium (2 mM). For 5.3-kHz imaging, data were averaged over 50 trials and reported as the change in fluorescence detected by HA10770-40 PMTs ($\Delta G/G$). In pointscan mode, the laser was parked at a single diffraction-limited spot and calcium and sodium influx were imaged with OGB-5N and ING-2, respectively, for 25 ms preceding and 100 ms following an AP. Fluorescence data were acquired at 20 kHz. Points were imaged in sets of five, each sampling a single AP, spaced at 0.5-μm intervals along the visualized edge of the axon. Individual points were imaged in a sequence of 2,4,1,3,5, with 2 being the point most proximal to the soma. Pointscans were imaged between 2 and 35 μm from the axon hillock. Individual APs within the set of five points were separated by 250 or 500 ms for calcium and sodium imaging, respectively. Data were averaged over 20–50 repetitions and then smoothed using a 40-point binomial filter in IgorPro before analysis.

Chemicals

TTA-P2 was from Alomone Labs. ω-Conotoxin-MVIIC, ω-conotoxin-GVIA, ω-agatoxin-TK, and SNX-482 were from Peptides International. Nifedipine was from Tocris. All calcium channel antagonists were prepared as stock solutions in ddH20 in glass vials. Ryanodine was from Tocris and was prepared as a stock solution (25 mM) in dimethylsulfoxide (DMSO; 0.08% final concentration DMSO). Peptide toxins were applied in recording solution supplemented with 1% bovine serum albumin to minimize peptide preabsorption. Recording solution reservoirs and tubing connecting the reservoir to the recording chamber were made of borosilicate glass, except for 30-mm lengths of Tygon tubing fed through the recirculation peristaltic pump (Ismatec Reglo). Alexa Fluor 594 hydrazide Na^+ salt, Fluo-5F pentapotassium salt, SBFI tetraammonium salt, Fluo-4FF pentapotassium salt, and Oregon Green 488 BAPTA-5N hexapotassium salt were from Invitrogen. ION NaTRIUM-Green-2 TMA+ salt (ING-2) was from Abcam.

Statistics

All data are reported as medians with interquartile ranges (IQR) in text and displayed with box plots (medians, quartiles and 90% tails) or violin

Table 1. Changes in AP waveform properties across the course of recording

	ΔV_m (mV)	$\Delta V_{threshold}$ (mV)	Δ AP half-width (% baseline)	Δ AP peak (mV)	Δ rheobase (pA)	n	Baseline EPSP (mV)	Postdrug EPSP (mV)
Time-locked control (15 min)	0.48 ± 1.05	-1.34 ± 1.86	98 ± 10	-3.23 ± 5.43	-10 ± 29.21	35	5.9 ± 4.6	4.6 ± 3.8
Conotoxin MVIIC	0.47 ± 0.54	-2.12 ± 1.55	99 ± 8	-3.12 ± 2.97	-21.43 ± 26.73	8	4.8 ± 3.8	$0.5 \pm 0.4*$
SNX-482	-0.18 ± 0.72	-0.92 ± 1.00	102 ± 11	-3.39 ± 5.00	-14.29 ± 19.67	8	—	—
TTA-P2	0.37 ± 0.65	-0.90 ± 0.88	100 ± 8	-3.02 ± 2.75	7.50 ± 37.36	11	—	—
Nifedipine	0.89 ± 0.42	-0.62 ± 1.42	102 ± 5	-3.12 ± 3.00	-8.33 ± 25.82	5	—	—
Conotoxin GVIA	0.14 ± 0.90	-0.78 ± 1.46	103 ± 5	-2.64 ± 1.17	-20.00 ± 20.92	5	5.3 ± 6.0	4.8 ± 5.5
Agatoxin TK	0.55 ± 0.42	-2.55 ± 0.84	104 ± 8	-2.70 ± 1.71	-12.50 ± 13.69	6	5.6 ± 4.1	$1.5 \pm 1.4*$
Ryanodine	1.49 ± 4.24	-1.14 ± 1.60	106 ± 11	-5.38 ± 5.62	-13.46 ± 24.19	14	—	—
Nickel(II) chloride	-0.26 ± 3.09	-0.51 ± 2.34	102 ± 5	-2.54 ± 2.58	-33.33 ± 43.78	6	—	—
Time-locked control (25 min)	0.54 ± 0.87	-3.25 ± 2.37	101 ± 7	-5.16 ± 3.71	-37.50 ± 37.91	6	3.7 ± 2.4	2.1 ± 0.8
Ca_V antagonist cocktail	0.37 ± 0.83	-3.26 ± 2.96	105 ± 4	-2.58 ± 6.08	-45.00 ± 32.60	5	2.5 ± 1.5	$0.5 \pm 0.4*$
S1 time-lock control	0.46 ± 0.96	-3.09 ± 2.07	96 ± 4	-2.57 ± 1.68	-8.33 ± 14.43	3	7.8 ± 2.5	7.2 ± 2.8
S1 conotoxin MVIIC	0.58 ± 2.57	-1.04 ± 1.84	98 ± 7	-6.09 ± 5.48	0 ± 86.60	3	6.0 ± 3.0	$0.7 \pm 0.4*$

$*p < 0.05$. One-way ANOVAs or two-tailed t tests were performed for each waveform property, as appropriate. Paired t tests were performed for EPSP amplitudes.

plots with individual data points overlaid. For linescan experiments, n denotes cells. For pointscan experiments, n denotes point sets, and the number of cells is reported in the text. For cells in Figures 1-3, time-locked control cells were interleaved with antagonist cells. Sample sizes were chosen based on standards in the field. No assumptions were made for data distributions, and unless otherwise noted, two-sided, rank-based nonparametric tests were used. Significance level was set for an α value of 0.05, and a Holm–Sidak correction was used for multiple comparisons when appropriate. Statistical analysis was performed using Statview, IgorPro 8.0, and the Real Statistic Resource Pack plugin for Microsoft Excel (Release 7.2).

Results

While AP-evoked Ca_V-mediated calcium influx has been observed in the AIS of a range of cell classes, the channels that mediate such influx appear to vary from class to class (Bender and Trussell, 2009; Yu et al., 2010; Martinello et al., 2015; Clarkson et al., 2017; Hanemaaijer et al., 2020). To determine the relative contributions of different calcium channel types during AP-evoked calcium influx in mouse prefrontal pyramidal cells, we made whole-cell current-clamp recordings from layer 5 pyramidal neurons in slices prepared from mice aged 20–30 d old. Neurons were filled via whole-cell dialysis with an internal solution containing Alexa Fluor 594 for morphological identification and the low-affinity calcium indicator Fluo-5F. The AIS was identified by the absence of spines and its stereotyped placement opposite the apical dendrite. Three APs were evoked by somatic current injection (1–1.5 nA, 5-ms duration, 20-ms inter-AP interval), and resultant AIS calcium influx was imaged in linescan mode ~30 µm from the axon hillock (Fig. 1A). AP-evoked calcium transients were stable over repeated linescan sets performed at time intervals used for subsequent pharmacological studies (median normalized peak $\Delta G/G_{sat}$ = 92.1% of baseline, interquartile range (IQR) = 88.4–104.4%, $n = 38$; Fig. 1B,D,E). This calcium influx was largely blocked by a cocktail of Ca_V antagonists that included blockers of Ca_V2.1, Ca_V2.2, Ca_V2.3, and Ca_V3 channels (1 µM ω-conotoxin MVIIC, 1 µm ω-conotoxin GVIA, 0.2 µM agatoxin TK, 0.5 µM SNX-482, 2 µM TTA-P2; median normalized peak $\Delta G/G_{sat}$ = 34.6%, IQR = 22.9–48.4%, $n = 7$, $p = 0.002$; Fig. 1B,D).

Specific channel antagonists were then applied one-by-one to examine contributions from individual Ca_V classes. Consistent with previous reports across a range of cell types (Bender and Trussell, 2009; Martinello et al., 2015; Clarkson et al., 2017; Fukaya et al., 2018), Ca_V3 channels were a substantial source of AIS calcium influx, as the specific antagonist TTA-P2 reduced

calcium influx to 76.6% of baseline (IQR = 75.0–84.9%, $n = 11$, $p = 0.002$, Mann–Whitney U test; Fig. 1C,E). Consistent with these results, application of 50 µM $NiCl_2$ caused a similar decrease in calcium influx (IQR = 77.5–86.9%, $n = 6$, $p = 0.004$; Fig. 1E). Additional contributions were made from Ca_V2 channels, with the Ca_V2.3-preferring antagonist SNX-482 reducing AIS calcium influx to 77.6% of baseline (500 nM; IQR = 72.4–88.4%, $n = 9$, $p = 0.005$; Fig. 1C,E). Application of the Ca_V2.1 channel antagonist ω-agatoxin-TK (200 nM) resulted in variable blockade, with AIS calcium unaffected in some cells and reduced ~30% in others (median: 74.1% of baseline, IQR = 68.6–91.9%, $n = 6$, $p = 0.067$; Fig. 1E). The Ca_V2.2 antagonist ω-conotoxin GVIA (1 µM) had little to no effect on AIS calcium (median = 88.9%, IQR = 85.6–91.3%, $n = 6$, $p = 0.137$; Fig. 1E), but the dual Ca_V2.1/2.2 antagonist ω-conotoxin MVIIC (1 µM) appeared to have an additive effect, blocking ~40% of total calcium influx (median normalized peak $\Delta G/G_{sat}$ = 61.5%, IQR = 58.3–73.0%, $n = 9$, $p = 4.03 \times 10^{-6}$; Fig. 1C,E). The presence of each of these Ca_V2.1/2.2 antagonists at the slice was confirmed by monitoring progressive blockade of evoked EPSPs elicited by a glass bipolar stimulating electrode placed 200 µm lateral to the soma in layer 5 (Table 1). Lastly, we applied the Ca_V1 antagonist nifedipine (10 µM), which had no effect on AIS calcium influx (median = 99.5%, IQR = 91.9–102.3%, $n = 7$, $p = 0.253$; Fig. 1E). We observed no change in AP peak, threshold, or half-width throughout the recordings (Table 1). Together, these data indicate that AP-evoked calcium influx in mouse prefrontal pyramidal cells is supported by a mix of Ca_V2 and Ca_V3 channels.

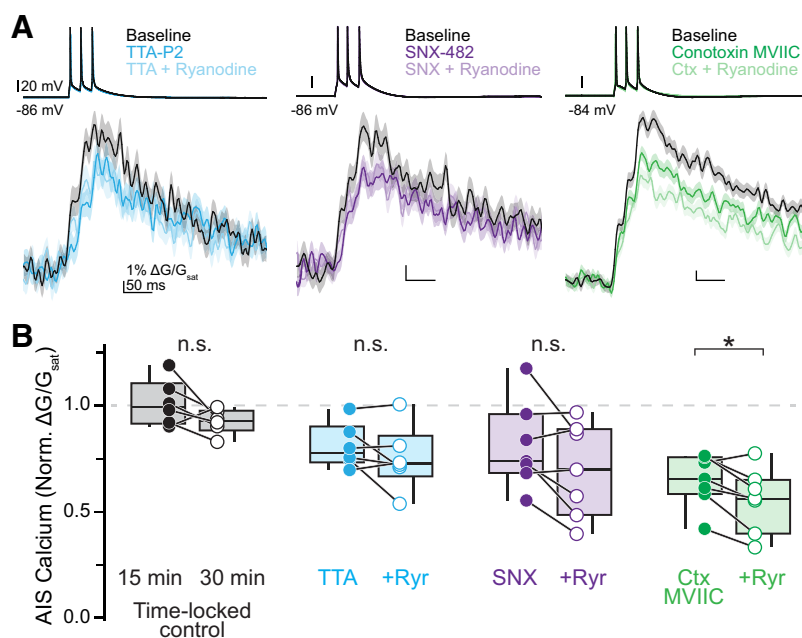## Ca_V3 channels couple to RyR-dependent stores at the AIS

Calcium-containing cisternal organelles are found in pyramidal cell initial segments throughout the neocortex (Benedeczky et al., 1994; Sánchez-Ponce et al., 2012; Antón-Fernández et al., 2015; Schlüter et al., 2017), but their role as a potential source of calcium during APs is not well understood. These cisternal organelles localize to discrete sites within the AIS of pyramidal cells (King et al., 2014; Schneider-Mizell et al., 2020) and express RyRs, which gate calcium-induced calcium release (Endo et al., 1970; Chamberlain et al., 1984; Van Petegem, 2012). Thus, they may boost AP-evoked calcium transients if they are coupled to Ca_Vs in the AIS. To determine whether calcium release from cisternal organelles is recruited at the AIS during AP generation, we began by comparing AP-evoked calcium influx at the AIS before and after ryanodine application, which at high concentrations (>10 µM) blocks calcium-induced calcium release by preventing

the opening of RyRs (Thomas and Williams, 2012). In contrast to somatosensory cortex layer 5b pyramidal neurons, where calcium stores account for ~50% of AP-evoked calcium transients (Hanemaaijer et al., 2020), ryanodine (20 μM) had a more modest effect in prefrontal cortex, reducing AP-evoked calcium transients to 85.4% of baseline (IQR = 79.2–89.4%, n = 17, p = 0.008; Fig. 2A,B). These RyR-dependent stores appear to be the sole source of intracellular calcium in the AIS, as subsequent application of the SERCA-ATPase inhibitor cyclopiazonic acid (CPA; 20 μM), which completely depletes calcium stores, did not lead to further decrements in AP-evoked calcium transients (ryanodine: 86.4% of baseline, IQR = 85.0–89.1%, ryanodine + CPA (30 min of application; Fig. 2A,C): 77.0% of baseline, IQR = 75.8–82.7%, n = 7, p = 0.108, Wilcoxon signed-rank test). This suggests that RyRs govern the majority of store-related calcium release during AP activity in the AIS.

RyRs can be coupled tightly to Ca$_V$s, either through direct physical coupling or through indirect nanodomain proximity (Johenning et al., 2015; Irie and Trussell, 2017). In the AIS, ryanodine-sensitive signaling is also important for D3 dopamine receptor-dependent regulation of Ca$_V$3s (Yang et al., 2016). To test whether RyR-dependent stores were preferentially coupled to particular Ca$_V$ classes present at the AIS, we performed sequential application of a selective Ca$_V$ antagonist followed by ryanodine (20 μM). With this approach, occlusion of any ryanodine-mediated reductions in AIS calcium would suggest that the blocked Ca$_V$ was the source of calcium that induced subsequent RyR-dependent store release. Interestingly, we found that block of Ca$_V$3 with TTA-P2 produced the clearest occlusion (TTA alone: median = 77.6%, IQR = 74.7–85.5%, TTA plus ryanodine = 72.5%, IQR = 71.2–78.9%, n = 6, p = 0.53, Wilcoxon signed-rank test; Fig. 3A,B). Conversely, application of ryanodine after preapplication of ω-conotoxin MVIIC resulted in a significant reduction in AIS calcium (conotoxin alone: median = 65.4%, IQR = 59.7–74.3%, conotoxin plus ryanodine: median = 56.1%, IQR = 47.4–62.8%, n = 7, p = 0.03, Wilcoxon signed-rank test; Fig. 3A,B). A mixed phenotype was observed with Ca$_V$2.3 block by SNX-482; decrements in calcium influx after ryanodine were observed in some cells, but the overall change was not significant (SNX alone: median = 73.8%, IQR = 70.3–89.8%, SNX plus ryanodine: median = 69.8%, IQR = 52.9–87.8%, n = 7, p = 0.20, Wilcoxon signed-rank test; Fig. 3A,B). Overall, these data indicate that, of all Ca$_V$ classes found in the AIS, Ca$_V$3s are
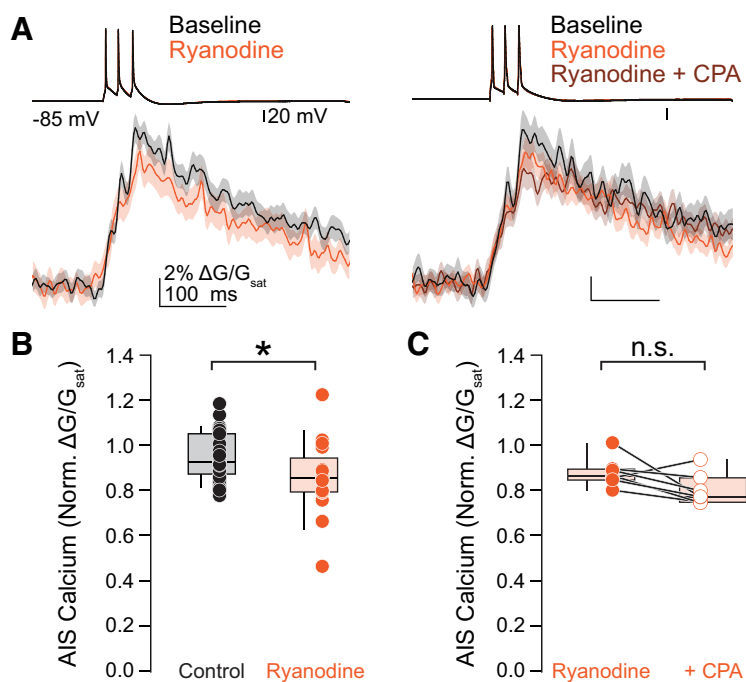
Figure 2. Calcium stores contribute to AIS calcium during AP firing. **A**, left, Representative effect of ryanodine (20 μM) on AIS calcium. Right, Representative effect of sequential ryanodine and CPA (20 μM) application on AIS calcium. Linescan data presented as mean ± SE. **B**, Summary of the effects of ryanodine on AIS calcium. *p < 0.05, Kruskal-Wallis with Mann-Whitney U test post hoc. **C**, Summary of the effects of sequential application of ryanodine and CPA. n.s.: not significant.

Figure 3. CaV3 channels couple to RyRs on calcium stores. **A**, Representative effects of sequential block of individual CaV types and release from calcium stores. Linescan data shown as mean ± SE. **B**, Summary of the effects of CaV antagonists and ryanodine block. n.s.: not significant. *p < 0.05, Wilcoxon signed-rank test.

most likely to be in close proximity to cisternal organelles to evoke release of calcium stores, although it is possible that Ca$_V$2.3s may also couple to RyRs.

Functional distribution of Ca$_V$3 and Ca$_V$2.1/2.2 in the AIS
RyRs are localized to discrete, ankyrin-G deficient regions of the AIS (King et al., 2014). Given the tight association between Ca$_V$3

channels and RyR-dependent release, we hypothesized that Ca_V3 channels may exhibit similar clustering at the functional level, which could be observed using approaches for resolving nanodomain hotspots of calcium. Such approaches have been used to examine discrete sites of calcium incursion at presynaptic terminals using confocal microscopy entry (DiGregorio et al., 1999; Nakamura et al., 2015) but, to our knowledge, have not been applied at the AIS with two-photon imaging.

To test whether there are sites within the AIS that are hotspots for calcium entry, the excitation laser was parked at one of five sites along the wall of the AIS membrane, each 500 nm apart, and APs were evoked while imaging calcium influx at 20 kHz. Calcium influx was reported with a recording solution containing the low-affinity calcium indicator Oregon Green BAPTA-5N (600 μM) supplemented with the slow calcium chelator EGTA (0.1 μM) to restrict imaged signals to sites experiencing rapid, high concentrations of calcium incursion (DiGregorio et al., 1999). The derivative of these events, which corresponds to the time in which calcium fluxes through channels (Sabatini and Regehr, 1999), corresponds to the rising phase of calcium transients (Fig. 4C). Data were quantified by comparing isochronal influx amplitude at the peak within the set of five points to the point (or average of points) 1 μm away on either flank. Using this approach, we identified a range of responses, from small differences across all five sites, to areas where certain locations had calcium incursions that were elevated relative to neighboring sites. In initial experiments that averaged over 50 trials, we found that the majority of sites (46 of 59 sites imaged across six cells) fell within a normal distribution (Fig. 4D), with no appreciable difference in peak calcium influx across all five sites. But in the remainder (13 of 59 sites across six cells; at least one site identified in each cell), calcium influx appeared to be more elevated and have sharper kinetics, consistent with a hotspot for calcium entry. Indeed, calcium entry at these sites was ~2× larger than in non-hotspot regions (Fig. 4E), while flanks 1 μm from the peak both more proximal or more distal to the axon hillock were of comparable amplitude to non-hotspot regions (Fig. 4F).

These hotspots may represent sites of concentrated calcium influx through Ca_Vs or reflect coupling to intracellular calcium stores. To test this, imaging was repeated (averages of 20 scans) in the presence of Ca_V3 antagonists, $Ca_V2.1/2.2$ antagonists, or with stores depleted with CPA. TTA-P2 (2 μM), $NiCl_2$ (50 μM), and conotoxin-MVIIC (1 μM) reduced overall calcium influx by 33.6%, 32.6%, and 17.1%, respectively (control median: 4.13 $\Delta G/G_{sat}$, IQR: 3.19–5.60, $n = 61$; TTA: 2.81, IQR: 2.37–3.66, $n = 50$; $NiCl_2$: 3.11, IQR: 2.76–3.46, $n = 28$; MVIIC 2.99, IQR: 2.39–4.26, $n = 36$). Co-application of TTA-P2, $NiCl_2$, and conotoxin-MVIIC reduced AP-evoked calcium transients below the level at which we could perform hotspot analysis [data not shown; average amplitude across five sites: 0.99 ± 0.11 G/G_{sat}; baseline root-mean-squared (RMS) noise per site: 1.78 ± 0.16, $n = 29$ sites over 5 cells]. By contrast, CPA had no effect on peak amplitude when compared with control sets acquired with identical approaches (CPA median: 3.88 IQR: 2.23–4.83, $n = 37$; Fig. 4G). This is consistent with the hypothesis that such imaging approaches using high concentrations of calcium indicators supplemented with calcium buffers may uncouple Ca_V-mediated influx from intracellular stores (Collier et al., 2000).

To determine whether Ca_V3 or $Ca_V2.1/2.2$ channels preferentially contribute to hotspot regions, amplitudes at the peak were compared with isochronal amplitudes 1 μm lateral for all data. To determine hotspot frequency after pharmacological manipulation, hotspots were defined as any set with a 1.5× difference

between the peak and 1 μm lateral amplitudes. While CPA had no effect on hotspot frequency, application of Ca_V antagonists changed hotspot frequency dramatically. Application of TTA-P2 or $NiCl_2$ eliminated hotspots almost entirely, whereas conotoxin-MVIIC increased the fraction of observed hotspots (Fig. 4H). Taken together, these data indicate that Ca_V3 channels are uniquely clustered in the AIS, producing nanodomains of elevated calcium entry that then couple to RyR-dependent stores. These regions likely account for hotspots that are eliminated on Ca_V3 block. By contrast, $Ca_V2.1/2.2$ channels appear to reside outside of hotspots, perhaps interspersed with ankyrin-G rich regions of AIS membrane. Consistent with this, hotspot frequency increases with $Ca_V2.1/2.2$ block, supporting the idea that hotspots are more easily resolved if calcium entry in non-hotspot regions is attenuated (e.g., greater signal-to-noise for resolving hotspots over valleys in between).

Temporally distinct AP-evoked sodium and calcium dynamics in the AIS

Imaging data above suggests that AIS calcium entry occurs during AP repolarization. While this is consistent with Ca_V activity during APs in a range of imaging and electrophysiological studies at various sites within the axon (DiGregorio et al., 1999; Bischofberger et al., 2002; Rowan et al., 2014; Díaz-Rojas et al., 2015; Nakamura et al., 2015), it has recently been proposed that AIS calcium influx during APs is mediated by Na_Vs, not Ca_Vs (Hanemaaijer et al., 2020). If this is the case, then calcium and sodium influx should occur simultaneously. To test this, we started by comparing AP-evoked sodium and calcium transients using 5.3-kHz linescans that transected the AIS 30 μm from the hillock. Linescans were collected at room temperature (22°C) to best separate the rising and falling phase of the AP. The low-affinity indicator Fluo-4FF was used for calcium imaging and the most commonly used sodium indicator, SBFI, was used for sodium imaging. SBFI reports changes in sodium concentration with a shift in emission spectra, which, with two-photon excitation sources, is best visualized as a reduction in fluorescence (Rose et al., 1999; Bender et al., 2010). Sodium and calcium transients were fitted with sigmoid functions and event onset was defined as the time at which the sigmoid fit first exceeded the amplitude of baseline RMS noise. Similar to previous reports (Hanemaaijer et al., 2020), we found that the rising slope of sodium and calcium transients were comparable (Na median = 0.07% $\Delta F/F$ per second, IQR = 0.06–0.08% $\Delta F/F$ per second, $n = 11$, Ca median = 0.07% $\Delta F/F$ per second, IQR = 0.04–0.08% $\Delta F/F$ per second, $n = 9$, $p = 0.6$, Mann–Whitney; Fig. 5B); however, sodium influx typically occurred during the rising phase of the AP, whereas calcium influx occurred during the falling phase (relative to AP peak, Na median = -0.343 ms, IQR = -0.4045–0.063 ms, $n = 11$ cells, Ca median = 0.901 s, IQR = 0.622–1.284, $n = 9$ cells, $p = 0.0007$, Mann–Whitney). The mean difference in transient onset was 1.2 ms, comparable to the duration of the rising phase of the AP in these recording conditions (median = 0.85 ms, IQR 0.76–0.94 ms, $n = 20$ cells).

SBFI typically reported ion influx with a higher signal-to-noise ratio than Fluo-4FF (peak amplitude/baseline RMS). This alone may account for the earlier event onset for SBFI-based signals. To test whether this was the case, we analyzed the subset of data in which signal-to-noise was comparable between sodium and calcium imaging scans (Fig. 5B). In these cases, sodium influx still preceded calcium influx. Thus, these data suggest that sodium and calcium influx occur through distinct mechanisms that can be separated temporally.
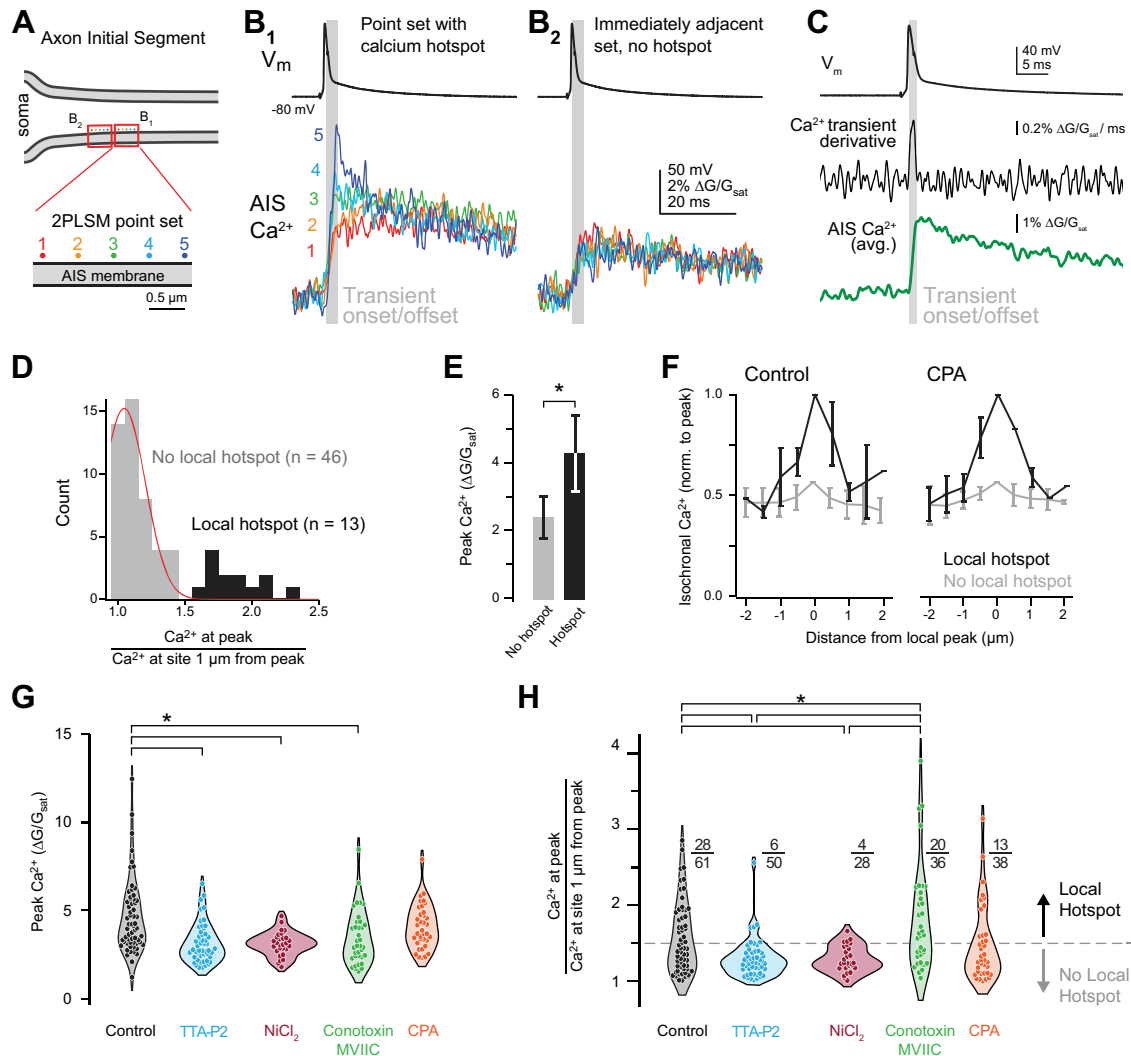
Figure 4. CaV3 channels and CaV2.1/2.2 exhibit distinct functional distributions. ***A***, Schematic of 2PLSM point scan imaging protocol. Points were imaged in sets of 5, with each point separated by 0.5 μm. The laser was parked at a single diffraction-limited point for 25 ms preceding and 100 ms following an AP and calcium influx was measured with OGB-5N. Points were scanned in the sequence 2, 4, 1, 3, 5 and each point sampled a single AP. Data were averaged over 20–50 repetitions. ***B***, Isochronal calcium peaks from neighboring point sets. Calcium influx at each point is color coded as in panel ***A***. ***B1*** shows a point set with a hotspot at point 5. ***B2*** is the point set immediately adjacent to ***B1*** and shows equivalent calcium influx across all points. Gray bar indicates the calcium transient onset and offset. ***C***, Average of calcium influx from a set of five points (bottom), its time derivative (middle), aligned to somatic voltage recording (top). Gray bar defines transient onset/offset, which corresponds to deviation of time derivative above baseline noise. ***D***, Distribution of point sets containing hotspots. Peak calcium influx at the brightest point was divided by the isochronal calcium influx at the point(s) 1 μm away. A total of 46 of 59 sites imaged fell within a normal distribution, while 13 sites exhibited higher relative calcium influx. Black, point sets containing a local hotspot; gray, point sets with no local hotspot. Red line indicates the fit of a normal distribution. Total distribution fit for normality (Shapiro–Wilk test *p* = 0.0016). ***E***, Calcium influx at hotspots was approximately 2× higher than calcium influx at non-hotspot points. Black, point sets containing a local hotspot; gray, point sets with no local hotspot. Data are plotted as mean ± SD. ***F***, Comparison of the flanks of point sets with a local hotspot and those without. Black, point sets containing a local hotspot; gray, point sets with no local hotspot. Data are plotted as mean ± SD for each 0.5-μm increment from the brightest point of the set. ***G***, Influence of selective CaV antagonists or store depletion on peak calcium influx during point scan imaging. Circles represent single point sets. Black, control; cyan, TTA-P2; red, NiCl2; green, *ω*-conotoxin MVIIC; orange, CPA; *∗p* < 0.001, Kruskall–Wallis test with rank-sum *post hoc*. ***H***, Influence of selective CaV antagonists or store depletion on calcium hotspots. Hotspots were classified as points >1.5 times brighter than the point(s) 1 μm away. Dotted gray line represents the distinction between point sets with a local hotspot (above) and those without (below). Color code as in panel ***F***; *∗p* < 0.001, Kruskall–Wallis test with rank-sum *post hoc*.

Previous work has suggested that the timing of calcium influx during an AP may shift to earlier parts of the AP at high temperature, in part because of differences in gating kinetics between Na_Vs and Ca_Vs (Sabatini and Regehr, 1996). This would be best assayed with the temporal fidelity of pointscan imaging. Unfortunately, we found the high basal fluorescence of SBFI resulted in significant photo-toxicity when the laser was parked at single sites. Therefore, we made use of a relatively new sodium-sensitive dye, ING-2, which reports increases in sodium concentration with an increase in fluorescence intensity without

a change in emission spectra (Filipis and Canepari, 2021). Sodium influx was imaged in sets of five sites each 0.5 μm apart, as done for calcium pointscan imaging. But in contrast to calcium imaging data, sodium influx did not appear to occur with regions that could be defined as hotspots. Rather, data reporting the relative amplitudes of the peak sodium transient relative to a neighbor 1 μm away could all be fit within a normal distribution (Shapiro–Wilk test for normality, *p* = 0.36; Fig. 6*B*,*C*), consistent with relatively constant Na_V density throughout the AIS (Kole et al., 2008; Lorincz and Nusser, 2008; Leterrier, 2018).
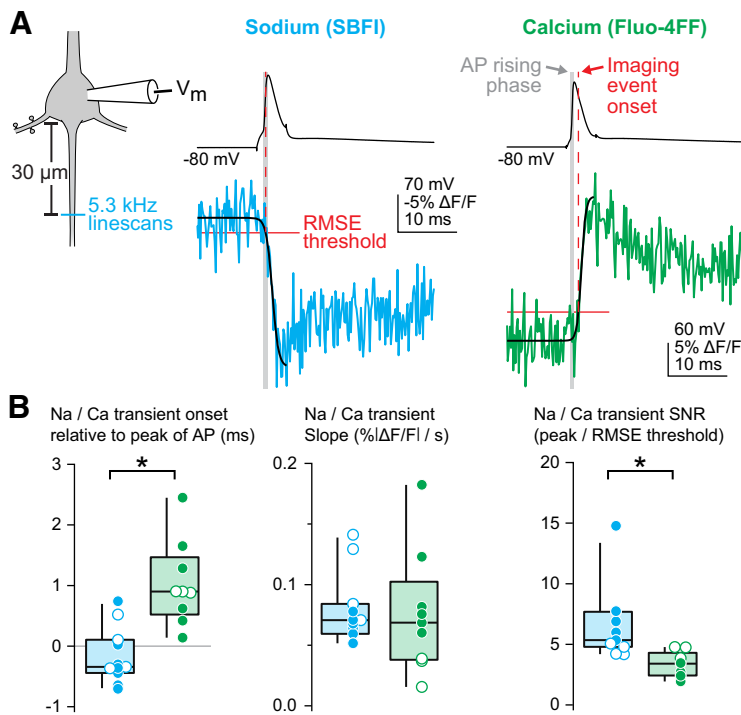
Figure 5. Fast linescan imaging reveals distinct temporal profiles of sodium and calcium influx. ***A***, Schematic of fast linescan protocol. Left, Linescan imaging was performed transecting the AIS at 5.3 kHz with either the sodium dye SBFI or the calcium dye Fluo-4FF. Middle, Representative example of sodium influx aligned to soma-evoked AP shows that sodium influx begins during the rising phase of the AP. Right, Representative example of calcium imaging aligned to AP. Calcium influx occurs during AP repolarization. Blue, SBFI; green, Fluo-4FF. Dashed vertical red line indicates imaging event onset. Gray bar represents rising phase of the AP (threshold to peak). Black line is the sigmoid fit of the linescan. Solid red line shows baseline noise of the linescan. ***B***, Comparison of sodium and calcium transient onset time, slope, and signal-to-noise ratio. Left, Summary of the timing of sodium and calcium transients relative to the peak of the AP. Negative values represent transient onset that precedes the AP peak. Middle, The slope of optically-recorded sodium and calcium transients. Slope was calculated using the sigmoid fit. Right, Signal-to-noise ratio for sodium and calcium transients. Circles represent individual cells. Open circles are cells with similar signal-to-noise ratios. Blue, SBFI; green, Fluo-4FF. *$p < 0.05$, Mann–Whitney U test.

Similar to data obtained at 22°C, sodium influx imaged 25–35 μm from the axon hillock again preceded the peak of the AP at 32–34°C (median = −0.65 ms, IQR = −0.9625 – −0.5 ms, n = 56 point sets, 23 cells). Moreover, these events tended to precede AP onset as measured in the soma (median = −0.05 ms, IQR = −0.3625–0.1 ms). This may be due in part to the conduction delay between the AIS site of AP initiation and the soma (Kole et al., 2007; Rowan et al., 2014; Spratt et al., 2021), and in part to subthreshold sodium influx before AP onset (Filipis and Canepari, 2021).

Comparisons with onset kinetics of calcium transients imaged with pointscan approaches again revealed marked differences between the onset of sodium and calcium entry. Calcium influx was detectable 1.2 ms after sodium influx, typically during the first millisecond of AP repolarization (median = 0.75, IQR = 0.60–1.35 ms after AP threshold, median = 0.35, IQR = 0.10–0.85 ms after AP peak, n = 38 sites, 13 cells; Fig. 6D). Similar results were obtained in conditions where Ca$_V$3 or Ca$_V$2.1/2.2 channels were blocked (TTA-P2: median = 1.1 ms, IQR = 0.8–1.6 ms after AP threshold, median = 0.6 ms, IQR = 0.3–1.1 ms after AP peak, n = 33 point sets, 7 cells; NiCl$_2$: median = 1.1 ms, IQR = 0.5–1.7 ms after AP threshold, median = 0.63 ms, IQR = 0.13–1.3 ms after AP peak, n = 28 point sets, 5 cells; ω-conotoxin MVIIC: median = 1.25 ms, IQR = 0.9625–1.575 ms after AP threshold, median = 0.7 ms, IQR = 0.375–1.1 ms after AP peak, n = 16 point

sets, 5 cells), and when intracellular stores were depleted with CPA (median = 0.7 ms, IQR = 0.4–0.9375 ms after AP threshold, median = 0.15 ms, IQR = −0.0375–0.4875 ms after AP peak, n = 20 point sets, 5 cells).

Overall, these data are most consistent with the hypothesis that Ca$_V$s are the sole source of calcium influx from the extracellular space in the AIS. This contrasts with work in rat somatosensory cortex (S1), where AP-evoked calcium transients were partially blocked by the Ca$_V$3 antagonist TTA-P2 (1 μM at equilibrium in the extracellular solution), but, notably, not affected by the Ca$_V$2 peptide antagonist ω-conotoxin MVIIC (2 μM, applied via pressure ejection local to the AIS; Hanemaaijer et al., 2020). Therefore, we tested whether mouse S1 pyramidal cells differ from mouse prefrontal pyramidal cells in the expression of Ca$_V$2.1/2.2 channels in the AIS by applying ω-conotoxin MVIIC (1 μM at equilibrium in the extracellular solution) to layer 5 pyramidal neurons in the somatosensory cortex, again imaging calcium influx resulting from three APs. Similar to mouse prefrontal cortex, block of Ca$_V$2.1/2.2 channels reduced peak calcium influx by over 35% (median = 63.8%, IQR = 42.5–69.9%, n = 5; time-locked controls: median = 90.9%, IQR = 79.6–95.5%, n = 5; p = 0.012, Mann–Whitney U test; Fig. 7A,B). Thus, these data indicate that pyramidal cells in multiple neocortical regions express a mix of Ca$_V$2 and Ca$_V$3 channels in their initial segments, at least in the mouse brain.

Discussion

Here, we show that calcium channels are functionally distributed in distinct domains within mouse prefrontal pyramidal cell initial segments. Low voltage-activated Ca$_V$3-mediated calcium influx occurs in spatially restricted hotspots, whereas high voltage-activated Ca$_V$2.1 and Ca$_V$2.2 channels provide a more diffuse source of calcium. Ca$_V$3-mediated hotspots preferentially evoke additional calcium release from RyR-dependent intracellular stores, suggesting that hotspots of Ca$_V$3-mediated influx localize to regions enriched with RyRs that are also sites for GABAergic input and K$_V$2.1 clustering (King et al., 2014). This suggests that different Ca$_V$ classes are functionally localized to discrete regions in the AIS.

Activity-dependent calcium sources in the AIS
Although AP-evoked calcium influx at the AIS is well established (Schiller et al., 1995; Callewaert et al., 1996), the sources of this calcium influx have only been investigated relatively recently. These sources appear to be remarkably heterogeneous across neuronal classes and species. In mouse auditory brainstem cartwheel cells, Ca$_V$3.2 and SNX-sensitive Ca$_V$2.3 account for ~90% of AP-evoked calcium influx, with no contributions from Ca$_V$2.1 or Ca$_V$2.2 (Bender and Trussell, 2009). By contrast, the first study of pyramidal cells in ferret neocortex found that calcium influx was mediated by Ca$_V$2.1 and Ca$_V$2.2 but not Ca$_V$3 (Yu et al., 2010). Here, we find that prefrontal pyramidal cells in mouse prefrontal cortex exhibit Ca$_V$3-mediated influx, consistent with previous reports in rodent neocortex (Clarkson et al., 2017; Hanemaaijer et al., 2020) and other brain regions (Gründemann
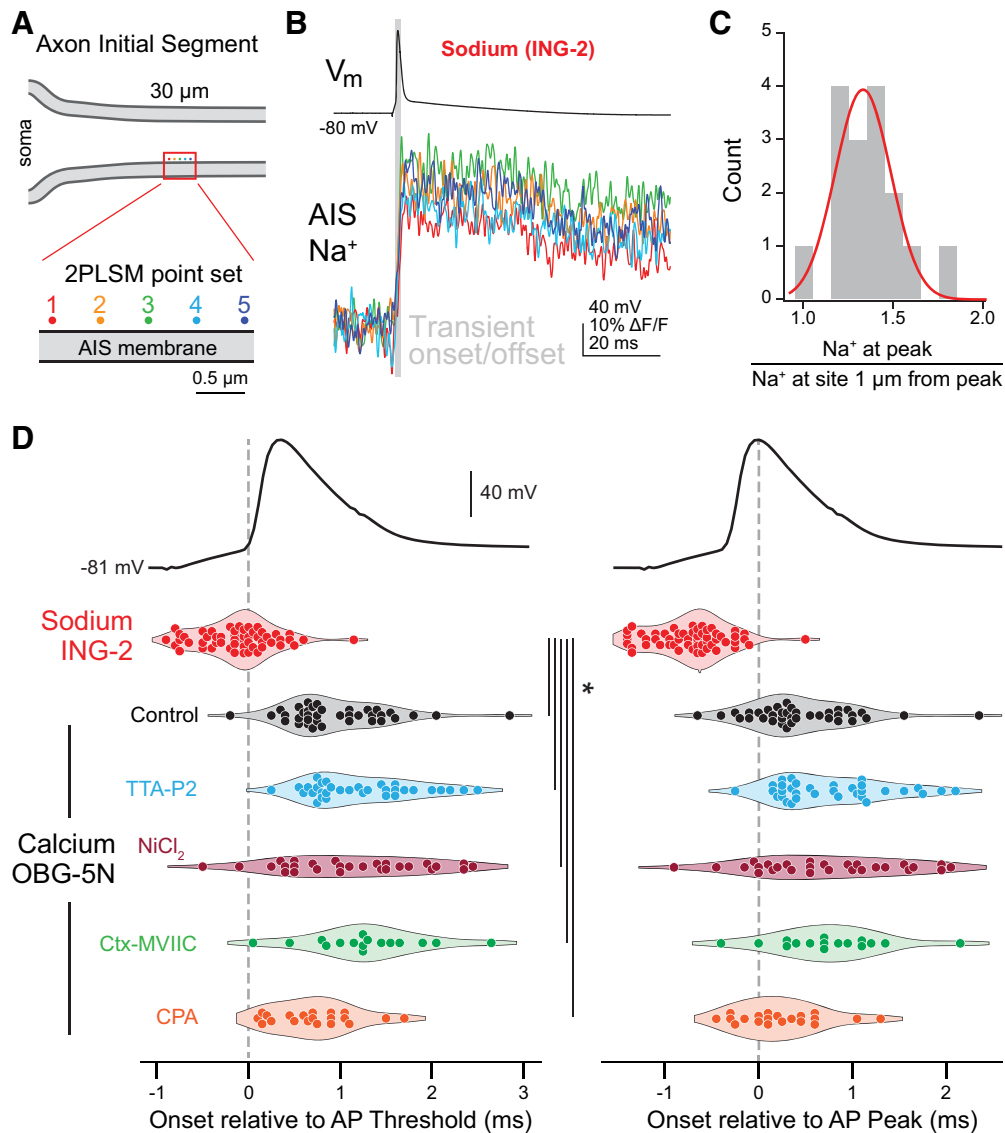
Figure 6. Sodium and calcium influx occur on the rising and falling phases of the AP at near-physiological temperatures, respectively. **A**, Pointscan imaging protocol was performed as in Figure 4A. OGB-5N was replaced with the sodium indicator ING-2, and Alexa Fluor 594 was excluded from the internal recording solution. **B**, Representative ING-2 sodium imaging pointset. Points are color-coded as in panel **A**. Gray bar indicates the sodium transient onset and offset. **C**, Distribution of sodium imaging point sets calculated as in Figure 4C. Red line represents the fit of a normal distribution to the data. **D**, Sodium and calcium transients from pointscan imaging temporally-aligned to AP threshold and peak. Left, Sodium and calcium influx onset relative to AP threshold. Right, Sodium and calcium influx onset relative to AP peak. Transient onset time was measured for the brightest point in a point set. Circles are individual point sets. Gray dashed line shows AP threshold (left) or peak (right) timing. Red, ING-2 sodium imaging; black, OGB-5N color coded as in Figure 4; ∗$p < 0.001$, Kruskall–Wallis test with rank-sum *post hoc*.

and Clark, 2015; Martinello et al., 2015; Jin et al., 2019). $Ca_V2.1/2.2$ and $Ca_V2.3$ were also found to contribute to calcium influx, highlighting the relative complexity of calcium signaling in prefrontal pyramidal cell initial segments.

In addition to CaV-mediated calcium influx, we found that a small fraction of AP-evoked calcium was released from ryanodine-sensitive intracellular stores in the AIS. Cisternal organelles at the AIS were proposed to be involved in calcium sequestration because of their expression of a calcium pump (Ca^{2+}-ATPase) in pyramidal neurons of the hippocampus (Benedeczky et al., 1994). Cisternal organelles were originally identified in the initial segments of cortical principal neurons in sensory cortical regions (Peters et al., 1968; Benedeczky et al., 1994). In these regions, a subpopulation of layer 5 pyramidal neurons contain a giant saccular organelle that extends through the entire AIS and accounts for a major fraction of AP-evoked calcium signals (Sánchez-Ponce et al., 2012; Antón-Fernández et al., 2015; Hanemaaijer et

al., 2020). Subsequent work has implicated both RyR-dependent and inositol 1,4,5-triphosphate (IP_3) receptor-dependent AIS-localized stores in a range of processes, including calcium influx during APs, modulation of AIS-associated proteins, and experience-dependent structural plasticity of the AIS compartment (Yang et al., 2016; Irie and Trussell, 2017; Schlüter et al., 2017; Gomez et al., 2020). These different effects may reflect diverse structures and functions in AIS calcium stores across cell types. Conversely, different modes of calcium release from intracellular stores may be recruited by different stimuli.

A recent study in rat somatosensory cortex layer 5b pyramidal cells found that a similar fraction of AP-evoked calcium signaling was sensitive to Ca_V3 antagonists, whereas inhibition of intracellular store calcium release reduced AP-evoked calcium transients to a far higher degree than observed here, consistent with the presence of giant saccular organelle in somatosensory cortical pyramidal neurons (Antón-Fernández et al., 2015; Hanemaaijer

A   Layer 5b pyramidal cells, somatosensory cortex
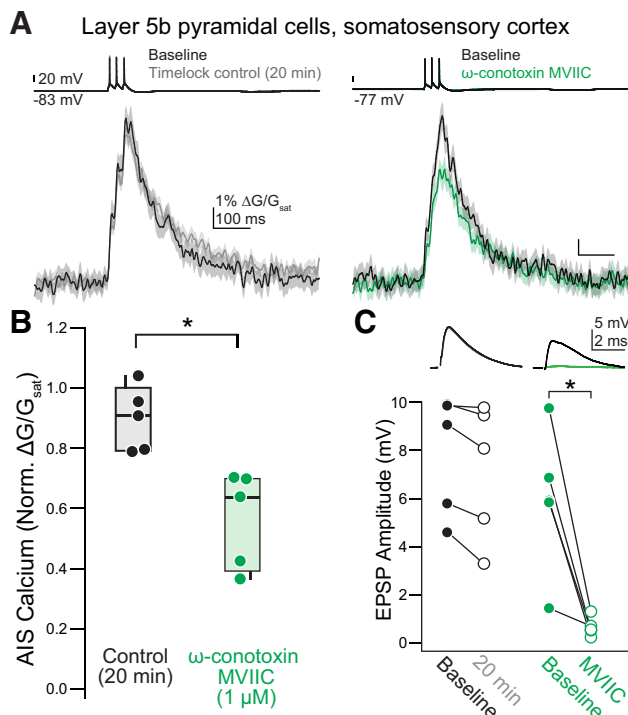
Figure 7. CaV2.1/2.2 contribute to AIS calcium in the somatosensory cortex. **A,** Representative effect of ω-conotoxin MVIIC application on AIS calcium in layer 5b pyramidal cells in the somatosensory cortex. Left, Example time-locked control cell. Black, baseline; gray, post. Right, Example of the effect of ω-conotoxin MVIIC. Black, baseline; green, ω-conotoxin MVIIC. Linescan data are plotted as mean $\pm$ SE. **B,** Summary of the effects of ω-conotoxin MVIIC on AIS calcium in somatosensory layer 5b pyramidal neurons. Black, time-locked control cells; green, ω-conotoxin MVIIC. $*p < 0.05$, Mann-Whitney U test. **C,** Decreases in EPSP amplitude confirm the presence of ω-conotoxin MVIIC at the slice. Top, Representative examples of EPSPs in ω-conotoxin MVIIC (right) or in time-locked control cells (left). Bottom, Summary of the effects of ω-conotoxin MVIIC on EPSP amplitude in somatosensory cortex. Black, baseline; gray, time-locked control; green, ω-conotoxin MVIIC. $*p < 0.05$, Mann-Whitney U test.

et al., 2020). Of note, peptide antagonists of $Ca_V2.x$ channels, puffed for 3s onto the AIS, did not affect AIS calcium influx, despite almost completely blocking AP-evoked calcium signals in axonal boutons. It was therefore proposed that the residual influx was through Na_Vs rather than Ca_Vs, based in part on the observations that influx was sensitive to Na_V antagonists and that the rising kinetics of sodium and calcium transients were similar (Hanemaaijer et al., 2020). Similar TTX-sensitivity has been observed previously for AIS calcium transients largely blocked by subthreshold depolarizations in auditory brainstem interneurons; however this sensitivity was attributed to a failure to activate AIS-localized Ca_Vs, rather than calcium influx through Na_Vs, as these transients could be blocked completely by Ca_V antagonists in the absence of TTX (Bender and Trussell, 2009).

In contrast to work in rat, we observed a marked block of AP-evoked influx in mouse prefrontal and somatosensory pyramidal cells from Ca_V2 antagonists when allowed to equilibrate in the extracellular solution (Figs. 1, 7). Furthermore, we found that the kinetics of sodium and calcium influx were indeed identical, but that calcium influx lagged sodium influx in ways that were consistent with sodium and calcium influx occurring on the rising and falling phases of the AP, respectively. These results are consistent with studies using high-speed optical imaging, where sodium influx occurs during the rising phase of the AP (Filipis and

Canepari, 2021), whereas calcium influx occurs during the falling phase of the AP in the AIS or AIS-like regions of AP initiation (Pressler and Strowbridge, 2019). Furthermore, we observed consistent results at both room temperature and physiological temperatures with two different sodium-sensitive indicators and two different calcium-sensitive indicators, suggesting that calcium influx occurs during Ca_V-mediated tail currents on the falling phase of the AP in the axon, regardless of temperature (Rowan et al., 2014; Kawaguchi and Sakaba, 2015; Pressler and Strowbridge, 2019; but see Sabatini and Regehr, 1996). Nevertheless, calcium influx, as assayed with synthetic indicators, could not be blocked completely with Ca_V antagonists. This may be because of several issues, including incomplete block of $Ca_V2.3$, or R-type calcium channels, so named for their resistance to antagonist block. Indeed, careful pharmacological studies across cell classes have shown that $Ca_V2.3$ channels in pyramidal cells are particularly resistant to block by SNX-482 (Sochivko et al., 2002). Furthermore, block of Ca_Vs by peptide toxins can have relatively slow kinetics (McDonough et al., 1996), and while we made every effort to allow for equilibration, with application times exceeding 20 min, this may not have been sufficient for complete block. Regardless, the kinetics of AIS calcium transients, observed here and in other reports (Figs. 5, 6; Pressler and Strowbridge, 2019), are most consistent with influx predominantly through Ca_Vs.

Functional compartmentalization of calcium influx within the AIS

In mature neocortical pyramidal cells, $Na_V1.6$ channels cluster in the regions of the AIS more distal to the soma, whereas $Na_V1.2$ channels cluster in the region more proximal to the soma (Hu et al., 2009). This subcompartmental distribution affects the integrative properties of the AIS in health and disease (Hu et al., 2009; Spratt et al., 2019), and raised the question of whether similar functional specializations are found in Ca_Vs localized to the AIS. To test this, we adapted spot imaging techniques used previously to observe calcium microdomains with single-photon sources for use with two-photon microscopy (DiGregorio et al., 1999; Nakamura et al., 2015). This approach revealed that calcium influx in the AIS occurs in two domains, with hotspots of calcium interspersed within regions of more consistent calcium influx (Fig. 4). These calcium nanodomains are hypothesized to result from channel clustering, as isochronal calcium measurements at increasing distances from the calcium source decreased in amplitude, a consequence of calcium diffusing away from its entry site (DiGregorio et al., 1999). It is plausible that the hotspots observed here represent points that are, by chance, closer to clusters of Ca_Vs; however, the differential pharmacological block of hotspots and non-hotspots with selective Ca_V antagonists indicates that these hotspots indeed reflect a differential organization of Ca_V channel types at the AIS. In future efforts, it will be important to develop immunostaining methods sensitive enough to visualize these channels relative to other AIS constituents to validate these functional observations.

The biophysics of different Ca_V channel types may shape calcium hotspot kinetics and duration as well. Relative to currents measured by step-commands, proportionally more current is carried by low voltage-activated than high voltage-activated channels during an AP waveform (McCobb and Beam, 1991). Low voltage-activated channels, including Ca_V3, can exhibit rapid activation kinetics when membrane voltage transitions quickly from rest to very depolarized potentials (e.g., during an AP; Chemin et al., 2001, 2002). As such, Ca_V3 channels open

earlier than other Ca$_V$ isoforms in the course of the AP, and, because of their slower deactivation kinetics, remain open longer than high voltage-activated channels, resulting in a longer duration of calcium influx through these channels (Lambert et al., 1998; McCobb and Beam, 1991). Hotspot calcium influx observed here is consistent with these biophysical aspects of AP-evoked Ca$_V$3-mediated currents.

Pharmacological block of RyR-dependent stores indicates that Ca$_V$3 channels couple to intracellular sources of calcium in the AIS. Ca$_V$2.3 channels may also couple to these stores, but data were less clear, perhaps because of incomplete block of Ca$_V$2.3 channels by SNX-482 (Sochivko et al., 2002). These RyR-dependent stores are found at ankyrin-G deficient regions of the axonal membrane (King et al., 2014), clustered with other AIS constituents. The components of the cytoskeletal scaffolding machinery that tether Na$_V$, K$_V$ channels, and GABA$_A$ receptors in the AIS have been well characterized (Leterrier, 2018), but how Ca$_V$s are anchored at the AIS remains an open question. One possibility, at least for Ca$_V$s clustered with RyRs, are K$_V$2.1 channels. K$_V$2.1 channels have been shown to tether Ca$_V$1 channels near junctions between the endoplasmic reticulum and plasma membrane (Fox et al., 2015), as well as to enhance the functional coupling of these channels to RyRs (Vierra et al., 2019). However, whether or not K$_V$2.1 channels tether Ca$_V$s near the cisternal organelle at the AIS specifically has not been explored. Another candidate is amphiphysin II/Bridging integrator 1 (BIN1), a T-tubule protein involved in localizing Ca$_V$1.2 channels in cardiac myocytes (Hong et al., 2010). This protein shows specific localization to neuronal AIS and nodes of Ranvier, but whether this protein interacts with AIS calcium channels has not been explored (Butler et al., 1997). Additionally, the presence of auxiliary subunits on Ca$_V$1 and Ca$_V$2 channels has been shown to affect localization and membrane expression (Arikkath and Campbell, 2003). As Ca$_V$3 channels do not associate with auxiliary subunits (Simms and Zamponi, 2014), Ca$_V$3 and Ca$_V$2 could acquire differential expression within the AIS through differential association of auxiliary subunits with scaffolding elements.

Functional implications of calcium channel compartmentalization within the AIS

GABA$_A$ receptors cluster in ankyrin-G deficient pockets of the AIS and associate with clustered non-conducting K$_V$2.1 channels that stabilize junctions between cisternal organelles and the plasma membrane (Benedeczky et al., 1994; King et al., 2014; Kirmiz et al., 2018; Schneider-Mizell et al., 2020). These clustering domains appear across species and brain regions (King et al., 2014). The coupling of Ca$_V$3 channels to RyRs, as well as the clustering of these channels into hotspots, suggests that Ca$_V$3 channels co-localize with GABAergic chandelier synapses in the AIS. Thus, AIS Ca$_V$3s may be particularly sensitive to chandelier cell input. In mature neurons, hyperpolarizing inhibition has been shown to relieve Ca$_V$3 channels from steady-state inactivation, thereby promoting rebound spike bursts immediately following an inhibitory epoch (Ulrich and Huguenard, 1997; Molineux et al., 2006). Interestingly, chandelier inputs switch from depolarizing to hyperpolarizing the AIS membrane relatively late in development (Rinetti-Vargas et al., 2017; Lipkin and Bender, 2020; Pan-Vazquez et al., 2020), corresponding to the emergence of synchronized higher-order rhythmicity in cortical networks (Uhlhaas and Singer, 2011). Whether this tight coupling between AIS GABAergic inputs and Ca$_V$3s contributes to the development of these network phenomena remains to be explored.

In addition to regulation by chandelier inputs, calcium hotspots could enable precise neuromodulatory control over spike properties, perhaps within select temporal windows relative to neuromodulator signals. In striatal medium spiny neurons, a form of credit assignment for synapses that encode information relevant to reward has been demonstrated based on coincident dopaminergic and glutamatergic signaling (Yagishita et al., 2014). In cells that express D3 dopamine receptors, including some prefrontal pyramidal cells, AIS Ca$_V$3 function can be modulated in ways that hyperpolarize the voltage dependence of channel inactivation, in turn lowering the number of channels available for activation during subsequent APs (Yang et al., 2016; Clarkson et al., 2017), This process depends on RyR-dependent intracellular stores (Yang et al., 2016). Thus, in D3 receptor-expressing neurons, Ca$_V$3 channels may be modulated only when dopamine binding to D3 receptors coincides with neuronal activity that promotes calcium influx through AIS Ca$_V$3s. This may result in preferential suppression of Ca$_V$3 function in cells that are actively spiking, thereby modulating only the population of neurons that were active during dopaminergic signaling.

References

Antón-Fernández A, Rubio-Garrido P, DeFelipe J, Muñoz A (2015) Selective presence of a giant saccular organelle in the axon initial segment of a sub-population of layer V pyramidal neurons. Brain Struct Funct 220:869–884.

Arikkath J, Campbell KP (2003) Auxiliary subunits: essential components of the voltage-gated calcium channel complex. Curr Opin Neurobiol 13:298–307.

Bender KJ, Trussell LO (2009) Axon initial segment Ca2+ channels influence action potential generation and timing. Neuron 61:259–271.

Bender KJ, Trussell LO (2012) The physiology of the axon initial segment. Annu Rev Neurosci 35:249–265.

Bender KJ, Ford CP, Trussell LO (2010) Dopaminergic modulation of axon initial segment calcium channels regulates action potential initiation. Neuron 68:500–511.

Bender KJ, Uebele VN, Renger JJ, Trussell LO (2012) Control of firing patterns through modulation of axon initial segment T-type calcium channels. J Physiol 590:109–118.

Benedeczky I, Molnár E, Somogyi P (1994) The cisternal organelle as a Ca (2+)-storing compartment associated with GABAergic synapses in the axon initial segment of hippocampal pyramidal neurones. Exp Brain Res 101:216–230.

Bischofberger J, Geiger JRP, Jonas P (2002) Timing and efficacy of Ca2+ channel activation in hippocampal mossy fiber boutons. J Neurosci 22:10593–10602.

Bock T, Stuart GJ (2016) The impact of BK channels on cellular excitability depends on their subcellular location. Front Cell Neurosci 10:206.

Bucurenciu I, Kulik A, Schwaller B, Frotscher M, Jonas P (2008) Nanodomain coupling between Ca2+ channels and Ca2+ sensors promotes fast and efficient transmitter release at a cortical GABAergic synapse. Neuron 57:536–545.

Burke KJ, Keeshen CM, Bender KJ (2018) Two forms of synaptic depression produced by differential neuromodulation of presynaptic calcium channels. Neuron 99:969–984.e7.

Butler MH, David C, Ochoa GC, Freyberg Z, Daniell L, Grabs D, Cremona O, De Camilli P (1997) Amphiphysin II (SH3p9; BIN1), a member of the amphiphysin/Rvs family, is concentrated in the cortical cytomatrix of axon initial segments and nodes of ranvier in brain and around T tubules in skeletal muscle. J Cell Biol 137:1355–1367.

Callewaert G, Eilers J, Konnerth A (1996) Axonal calcium entry during fast "sodium" action potentials in rat cerebellar Purkinje neurones. J Physiol 495:641–647.

Chamberlain BK, Volpe P, Fleischer S (1984) Inhibition of calcium-induced calcium release from purified cardiac sarcoplasmic reticulum vesicles. J Biol Chem 259:7547–7553.

Chemin J, Monteil A, Bourinet E, Nargeot J, Lory P (2001) Alternatively spliced α1G (Cav3.1) Intracellular loops promote specific T-type Ca2+ channel gating properties. Biophys. J 80:1238–1250.

Chemin J, Monteil A, Perez -Reyes E, Bourinet E, Nargeot J, Lory P (2002) Specific contribution of human T-type calcium channel isotypes (α_{1G}, α_{1H} and α_{1I}) to neuronal excitability. J Physiol 540:3–14.

Chen-Engerer HJ, Hartmann J, Karl RM, Yang J, Feske S, Konnerth A (2019) Two types of functionally distinct Ca2+ stores in hippocampal neurons. Nat Commun 10:3223.

Clarkson RL, Liptak AT, Gee SM, Sohal XVS, Bender XKJ (2017) D3 Receptors regulate excitability in a unique class of prefrontal pyramidal cells. J Neurosci 37:5846–5860.

Collier ML, Ji G, Wang YX, Kotlikoff MI (2000) Calcium-induced calcium release in smooth muscle: loose coupling between the action potential and calcium release. J Gen Physiol 115:653–662.

Díaz-Rojas F, Sakaba T, Kawaguchi SY (2015) Ca(2+) current facilitation determines short-term facilitation at inhibitory synapses between cerebellar Purkinje cells. J Physiol 593:4889–4904.

DiGregorio DA, Peskoff A, Vergara JL (1999) Measurement of action potential-induced presynaptic calcium domains at a cultured neuromuscular junction. J Neurosci 19:7846–7859.

Dumenieu M, Senkov O, Mironov A, Bourinet E, Kreutz MR, Dityatev A, Heine M, Bikbaev A, Lopez-Rojas J (2018) The low-threshold calcium channel Cav3.2 mediates burst firing of mature dentate granule cells. Cereb Cortex 28:2594–2609.

Endo M, Tanaka M, Ogawa Y (1970) Calcium induced release of calcium from the sarcoplasmic reticulum of skinned skeletal muscle fibres. Nature 228:34–36.

Filipis L, Canepari M (2021) Optical measurement of physiological sodium currents in the axon initial segment. J Physiol 599:49–66.

Fox PD, Haberkorn CJ, Akin EJ, Seel PJ, Krapf D, Tamkun MM (2015) Induction of stable ER-plasma-membrane junctions by Kv2.1 potassium channels. J Cell Sci 128:2096–2105.

Fukaya R, Yamada R, Kuba H (2018) Tonotopic variation of the T-type Ca2+ current in avian auditory coincidence detector neurons. J Neurosci 38:335–346.

Gomez LC, Kawaguchi SY, Collin T, Jalil A, del Pilar Gomez M, Nasi E, Marty A, Llano I (2020) Influence of spatially segregated IP3-producing pathways on spike generation and transmitter release in Purkinje cell axons. Proc Natl Acad Sci USA 117:11097–11108.

Gründemann J, Clark BA (2015) Calcium-activated potassium channels at nodes of Ranvier secure axonal spike propagation. Cell Rep 12:1715–1722.

Hanemaaijer NA, Popovic MA, Wilders X, Grasman S, Pavón Arocas O, Kole MH (2020) Ca2+ entry through NaV channels generates submillisecond axonal Ca2+ signaling. Elife 9:e54566.

Hong TT, Smyth JW, Gao D, Chu KY, Vogan JM, Fong TS, Jensen BC, Colecraft HM, Shaw RM (2010) BIN1 localizes the L-type calcium channel to cardiac T-tubules. PLoS Biol 8:e1000312.

Hu W, Bean BP (2018) Differential control of axonal and somatic resting potential by voltage-dependent conductances in cortical layer 5 pyramidal neurons. Neuron 97:1315–1326.e3.

Hu W, Tian C, Li T, Yang M, Hou H, Shu Y (2009) Distinct contributions of Na(v)1.6 and Na(v)1.2 in action potential initiation and backpropagation. Nat Neurosci 12:996–1002.

Huang CYM, Rasband MN (2018) Axon initial segments: structure, function, and disease. Ann NY Acad Sci 1420:46–61.

Inan M, Anderson SA (2014) The chandelier cell, form and function. Curr Opin Neurobiol 26:142–148.

Irie T, Trussell LO (2017) Double-nanodomain coupling of calcium channels, ryanodine receptors, and BK channels controls the generation of burst firing. Neuron 96:856–870.e4.

Jin X, Chen Q, Song Y, Zheng J, Xiao K, Shao S, Fu Z, Yi M, Yang Y, Huang Z (2019) Dopamine D2 receptors regulate the action potential threshold by modulating T-type calcium channels in stellate cells of the medial entorhinal cortex. J Physiol 597:3363–3387.

Jing M, Zhang P, Wang G, Feng J, Mesik L, Zeng J, Jiang H, Wang S, Looby JC, Guagliardo NA, Langma LW, Lu J, Zuo Y, Talmage DA, Role LW, Barrett PQ, Zhang LI, Luo M, Song Y, Zhu JJ, et al. (2018) A genetically encoded fluorescent acetylcholine indicator for in vitro and in vivo studies. Nat Biotechnol 36:726–737.

Johenning FW, Theis A-K, Pannasch U, Rückl M, Rüdiger S, Schmitz D (2015) Ryanodine receptor activation induces long-term plasticity of spine calcium dynamics. PLoS Biol 13:e1002181.

Jones SL, Stuart GJ (2013) Different calcium sources control somatic versus dendritic SK channel activation during action potentials. J Neurosci 33:19396–19405.

Kawaguchi SY, Sakaba T (2015) Control of inhibitory synaptic outputs by low excitability of axon terminals revealed by direct recording. Neuron 85:1273–1288.

King AN, Manning CF, Trimmer JS (2014) A unique ion channel clustering domain on the axon initial segment of mammalian neurons. J Comp Neurol 522:2594–2608.

Kirmiz M, Palacio S, Thapa P, King AN, Sack JT, Trimmer JS (2018) Organizing neuronal ER-PM junctions is a conserved nonconducting function of Kv2 plasma membrane ion channels. Mol Biol Cell 29:2410–2432.

Kole MHP, Stuart GJ (2012) Signal processing in the axon initial segment. Neuron 73:235–247.

Kole MHP, Letzkus JJ, Stuart GJ (2007) Axon initial segment Kv1 channels control axonal action potential waveform and synaptic efficacy. Neuron 55:633–647.

Kole MHP, Ilschner SU, Kampa BM, Williams SR, Ruben PC, Stuart GJ (2008) Action potential generation requires a high sodium channel density in the axon initial segment. Nat Neurosci 11:178–186.

Lambert RC, McKenna F, Maulet Y, Talley EM, Bayliss DA, Cribbs LL, Lee JH, Perez-Reyes E, Feltz A (1998) Low-voltage-activated Ca2+ currents are generated by members of the Ca(v)T subunit family (alpha1G/H) in rat primary sensory neurons. J Neurosci 18:8605–8613.

Leterrier C (2018) The axon initial segment: an updated viewpoint. J Neurosci 38:2135–2145.

Leterrier C, Dargent B (2014) No Pasaran! Role of the axon initial segment in the regulation of protein transport and the maintenance of axonal identity. Semin Cell Dev Biol 27:44–51.

Lipkin AM, Bender KJ (2020) Flipping the switch: homeostatic tuning of chandelier synapses follows developmental changes in GABA polarity. Neuron 106:199–201.

Lorincz A, Nusser Z (2008) Cell-type-dependent molecular composition of the axon initial segment. J. Neurosci 26:7172–7180.

Martinello K, Huang Z, Lujan R, Tran B, Watanabe M, Cooper EC, Brown DA, Shah MM (2015) Cholinergic afferent stimulation induces axonal function plasticity in adult hippocampal granule cells. Neuron 85:346–363.

McCobb DP, Beam KG (1991) Action potential waveform voltage-clamp commands reveal striking differences in calcium entry via low and high voltage activated calcium channels. Neuron 7:119–127.

McDonough SI, Swartz KJ, Mintz IM, Boland LM, Bean BP (1996) Inhibition of calcium channels in rat central and peripheral neurons by omega-conotoxin MVIIC. J Neurosci 16:2612–2623.

Molineux ML, Mcrory JE, Mckay BE, Hamid J, Mehaffey WH, Rehak R, Snutch TP, Zamponi GW, Turner RW (2006) Specific T-type calcium channel isoforms are associated with distinct burst phenotypes in deep cerebellar nuclear neurons. Proc Natl Acad Sci USA 103:5555–5560.

Nakamura Y, Harada H, Kamasawa N, Matsui K, Rothman JS, Shigemoto R, Silver RA, DiGregorio DA, Takahashi T (2015) Nanoscale distribution of presynaptic Ca(2+) channels and its impact on vesicular release during development. Neuron 85:145–158.

Ogawa Y, Rasband MN (2008) The functional organization and assembly of the axon initial segment. Curr Opin Neurobiol 18:307–313.

Pan-Vazquez A, Wefelmeyer W, Gonzalez Sabater V, Neves G, Burrone J (2020) Activity-dependent plasticity of axo-axonic synapses at the axon initial segment. Neuron 106:265–276.e6.

Peters A, Proskauer CC, Kaiserman-Abramof IR (1968) The small pyramidal neuron of the rat cerebral cortex. The axon hillock and initial segment. J Cell Biol 39:604–619.

Pinatel D, Hivert B, Saint-Martin M, Noraz N, Savvaki M, Karagogeos D, Faivre-Sarrailh C (2017) The Kv1-associated molecules TAG-1 and Caspr2 are selectively targeted to the axon initial segment in hippocampal neurons. J Cell Sci 130:2209–2220.

Pressler RT, Strowbridge BW (2019) Functional specialization of interneuron dendrites: identification of action potential initiation zone in axonless olfactory bulb granule cells. J Neurosci 39:9674–9688.

Rebola N, Reva M, Kirizs T, Szoboszlay M, Lőrincz A, Moneron G, Nusser Z, DiGregorio DA (2019) Distinct nanoscale calcium channel and synaptic vesicle topographies contribute to the diversity of synaptic function. Neuron 104:693–710.e9.

Rinetti-Vargas G, Phamluong K, Ron D, Bender KJ (2017) Periadolescent maturation of GABAergic hyperpolarization at the axon initial segment. Cell Rep 20:21–29.

Rose CR, Kovalchuk Y, Eilers J, Konnerth A (1999) Two-photon Na+ imaging in spines and fine dendrites of central neurons. Pflügers Arch 439:201–207.

Rowan MJM, Tranquil E, Christie JM (2014) Distinct Kv channel subtypes contribute to differences in spike signaling properties in the axon initial segment and presynaptic boutons of cerebellar interneurons. J Neurosci 34:6611–6623.

Sabatini BL, Regehr WG (1996) Timing of neurotransmission at fast synapses in the mammalian brain. Nature 384:170–172.

Sabatini BL, Regehr WG (1999) Timing of synaptic transmission. Annu Rev Physiol 61:521–542.

Sánchez-Ponce D, Blázquez-Llorca L, Defelipe J, Garrido JJ, Muñoz A (2012) Colocalization of α-actinin and synaptopodin in the pyramidal cell axon initial segment. Cereb Cortex 22:1648–1661.

Schiller J, Helmchen F, Sakmann B (1995) Spatial profile of dendritic calcium transients evoked by action potentials in rat neocortical pyramidal neurones. J. Physiol 487:583–600.

Schlüter A, Del Turco D, Deller T, Gutzmann A, Schultz C, Engelhardt M (2017) Structural plasticity of synaptopodin in the axon initial segment during visual cortex development. Cereb Cortex 27:4662–4675.

Schneider-Mizell CM, Bodor AL, Collman F, Brittain D, Bleckert AA, Dorkenwald S, Turner NL, Macrina T, Lee K, Lu R, Wu J, Zhuang J, Nandi A, Hu B, Buchanan J, Takeno MM, Torres R, Mahalingam G, Bumbarger DJ, Li Y, et al. (2020) Chandelier cell anatomy and function reveal a variably distributed but common signal. bioRxiv. doi: 10.1101/2020.03.31.018952.

Scimemi A, Diamond JS (2012) The number and organization of Ca2+ channels in the active zone shapes neurotransmitter release from Schaffer collateral synapses. J Neurosci 32:18157–18176.

Simms BA, Zamponi GW (2014) Neuronal voltage-gated calcium channels: structure, function, and dysfunction. Neuron 82:24–45.

Sochivko D, Pereverzev A, Smyth N, Gissel C, Schneider T, Beck H (2002) The Ca(V)2.3 Ca(2+) channel subunit contributes to R-type Ca2+ currents in murine hippocampal and neocortical neurones. J Physiol 542:699–710.

Spratt PWE, Ben-Shalom R, Keeshen CM, Burke KJ, Clarkson RL, Sanders SJ, Bender KJ (2019) The autism-associated gene Scn2a contributes to dendritic excitability and synaptic function in the prefrontal cortex. Neuron 103:673–685.e5.

Spratt PWE, Ben-Shalom R, Sahagun A, Keeshen CM, Sanders SJ, Bender KJ (2021) Paradoxical hyperexcitability from NaV1.2 sodium channel loss in neocortical pyramidal cells. bioRxiv. doi: 10.1101/2021.02.02.429423.

Thomas NL, Williams AJ (2012) Pharmacology of ryanodine receptors and Ca2+-induced Ca2+ release. WIREs Membr Transp Signal 1:383–397.

Uhlhaas PJ, Singer W (2011) The development of neural synchrony and large-scale cortical networks during adolescence: relevance for the pathophysiology of schizophrenia and neurodevelopmental hypothesis. Schizophr Bull 37:514–523.

Ulrich D, Huguenard JR (1997) Nucleus-specific chloride homeostasis in rat thalamus. J Neurosci 17:2348–2354.

Van Petegem F (2012) Ryanodine receptors: structure and function. J Biol Chem 287:31624–31632.

Vierra NC, Kirmiz M, List D, Van Der Santana LF, Trimmer JS (2019) Kv2.1 mediates spatial and functional coupling of L-type calcium channels and ryanodine receptors in mammalian neurons. Elife 8:e49953.

Vyleta NP, Jonas P (2014) Loose coupling between Ca2+ channels and release sensors at a plastic hippocampal synapse. Science 343:665–670.

Wang K, Lin MT, Adelman JP, Maylie J (2014) Distinct Ca2+ sources in dendritic spines of hippocampal CA1 neurons couple to SK and Kv4 channels. Neuron 81:379–387.

Wheeler DG, Groth RD, Ma H, Barrett CF, Owen SF, Safa P, Tsien RW (2012) Ca(V)1 and Ca(V)2 channels engage distinct modes of Ca(2+) signaling to control CREB-dependent gene expression. Cell 149:1112–1124.

Yagishita S, Hayashi-Takagi A, Ellis-Davies GCR, Urakubo H, Ishii S, Kasai H (2014) A critical time window for dopamine actions on the structural plasticity of dendritic spines. Science 345:1616–1620.

Yang S, Ben-Shalom R, Ahn M, Liptak ATAT, van Rijn RMRM, Whistler JLJL, Bender KJKJ (2016) β-Arrestin-dependent dopaminergic regulation of calcium channel activity in the axon initial segment. Cell Rep 16:1518–1526.

Yu Y, Maureira C, Liu X, Mccormick D (2010) P/Q and N channels control baseline and spike-triggered calcium levels in neocortical axons and synaptic boutons. J Neurosci 30:11858–11869.